International Journal of Hydrogen Energy 105 (2025) 1153–1163

Contents lists available at ScienceDirect

International Journal of Hydrogen Energy

journal homepage: www.elsevier.com/locate/he

Facet-dependent reaction mechanism of Fe-based oxygen carrier for CH_4 chemical looping combustion

Junchang Xiong [a,c], Meirong Dong [a,c,*], Zehua Huang [a,c], Hongchuan Liu [a,c], Huaming Hou [b], Youcai Liang [a,c], Jidong Lu [a,c]

[a] School of Electric Power, South China University of Technology, Guangzhou, Guangdong, 510640, China
[b] National Energy Center for Coal to Clean Fuels, Synfuels China Technology Co., Ltd., Beijing, 101407, China
[c] Guangdong Province Engineering Research Center of High Efficient and Low Pollution Energy Conversion, Guangzhou, Guangdong, 510640, China

ARTICLE INFO

Handling Editor: Søren Juhl Andreasen

Keywords:
Chemical-looping combustion
Fe-based oxygen carrier
Crystal facet-dependent
Reaction mechanism

ABSTRACT

Chemical looping combustion (CLC) technology decouples the traditional combustion process into two gas-solid reactions. The crystal facet effect is a crucial factor in gas-solid reactions. However, the chemical looping combustion mechanism associated with the crystal facet remains unclear. In this work, we investigated Fe_2O_3 crystal facet on the performance and reaction mechanism of CH_4 chemical looping. Hex-, cubic and rh-like Fe_2O_3 with predominantly exposed (001), (012), and (104) facets were prepared, and their properties were tested in a fixed bed, respectively. The results show that the reactivity of Fe_2O_3 exhibits a clear facet dependence, with the order of reactivity being (104)>(012)>(001), which correlates with the high reactive oxygen content on the corresponding facet by X-ray photoelectron spectroscopy (XPS). Density functional theory (DFT) calculations further confirm that Fe_2O_3(104) exhibits the lowest oxygen vacancy formation energy, providing a favorable low energy barrier channel for lattice oxygen migration. The differences in crystallographic surfaces leads to an upward shift of the O-2p band of the oxygen carriers, enhancing the lattice oxygen activity. Moreover, molecular dynamics and detailed reaction pathways indicate that the rate-determining step (RDS) for Fe_2O_3(001) and Fe_2O_3(012) is the oxidation of methoxy, whereas the RDS for Fe_2O_3(104) is the oxidation of formate with a lower activation energy barrier. The facet-dependent oxygen mobility and reaction pathways result in a distinct catalytic performance for chemical looping combustion of CH_4. This study presents a general strategy based on facet engineering to improve the performance of oxygen carriers.

1. Introduction

Carbon dioxide (CO_2), the most significant greenhouse gas contributing to global warming and climate change, necessitates a substantial reduction in atmospheric concentrations. Enhancing energy efficiency and increasing the use of low- or zero-carbon energy sources, such as biofuels, are effective strategies for reducing carbon dioxide emissions at their source [1]. Additionally, employing negative emission technologies to directly remove carbon dioxide from the atmosphere and store it represents another promising approach [2]. However, the potential environmental impacts of large-scale implementation of these technologies warrant careful consideration. To tackle the urgent challenge of climate change, Carbon Capture, Utilization, and Storage (CCUS) emerges as a vital and reliable technology, poised to play a crucial role in carbon reduction efforts. Nevertheless, CCUS is hindered by the high costs associated with air separation. Fortunately, the innovative technology of Chemical Looping Combustion (CLC) offers a solution to this challenge.

CLC is an innovative energy utilization method that inherently separates CO_2, reduces NOx emissions, and utilizes energy cascades. It is regarded as a cost-effective solution for CO_2 reduction. In CLC process, the oxygen carrier supplies oxygen to the fuel molecules in the fuel reactor to facilitate combustion. Subsequently, the depleted oxygen carrier undergoes oxidation and regeneration in the air reactor before being transferred back to the fuel reactor for the subsequent cycle. The replacement of gas-phase oxygen with the oxygen carrier ensures effective separation between gas and solid phases. This process guarantees that the CO_2 produced at the outlet of the fuel reactor can be captured at a minimal energy cost, while also generating heat. It is therefore imperative to gain a comprehensive understanding of the

* Corresponding author. School of Electric Power, South China University of Technology, Guangzhou, Guangdong, 510640, China.
E-mail address: epdongmr@scut.edu.cn (M. Dong).

https://doi.org/10.1016/j.ijhydene.2025.01.342
Received 10 September 2024; Received in revised form 15 January 2025; Accepted 21 January 2025
Available online 31 January 2025

selection of oxygen carrier materials, as well as the evolutionary behavior and intrinsic mechanisms of the thermochemical processes in oxygen carriers, in order to achieve the realization of the chemical looping system.

As a complex multiphase reaction, chemical looping combustion takes place at the surface interface between the oxygen carrier and the reacting gas, accompanied by the migration of bulk oxygen. Therefore, the exposed crystalline surfaces of the oxygen carrier play a dominant role in the oxidation of the gaseous fuels. The arrangement and coordination of atoms on different exposed surfaces results in differences in the physicochemical properties of the material, such as specific surface area, lattice oxygen activity and adsorption behavior. Jian et al. [3]. found that the presence of a large amount of Lewis acid base in Rod-like Co_3O_4 with (110) facet accelerated the activation of the C–H bond and promoted the oxidation of propane compared to Co_3O_4 (111) and Co_3O_4 (100). Zhao et al. [4]. found that the Bi_2MoO_6(001) crystalline surface has better bulk phase oxygen mobility than Bi_2MoO_6(010). The difference in oxygen mobility leads to a complex side reaction in the oxidation of 1-butene in Bi_2MoO_6(010) due to insufficient oxygen supply, which hinders the selective oxidation of 1-butene. Cao et al. [5]. investigated the effect of Mn_2O_3 exposed crystal surfaces on the oxidation reaction of NO and found that NO follows the Langmuir-Hinshelwood oxidation mechanism on Mn_2O_3(220) and (400), whereas it follows the Mars-van-Krevelen mechanism on Mn_2O_3(222). These studies have shown that exposing the crystal surface often leads to a change in the lattice oxygen activity as well as changes in reaction mechanism and pathway. It is therefore considered that enhancing the lattice oxygen activity by adjusting the morphology of the oxygen carriers and exposing the crystal surface is an effective way approach to increase the catalytic oxidation activity of chemical looping.

CH_4 Chemical looping combustion(CH_4-CLC) is seen as an important solution to address both energy use and environmental harmony [6,7]. As CLC technology, employing a variety of oxygen carriers, remains in the developmental stage, a significant number of oxygen carriers have been examined [8]. Natural hematite, which is mainly composed of Fe_2O_3, is a widely used oxygen carrier due to its low cost and the fact that it is environmentally friendly [9]. The reactivity of hematite is related to the valence multiplicity of Fe species, which readily activate CH_4 and release lattice oxygen to participate in oxidation. Despite efforts have been made to develop highly active and selective Fe-based oxygen carriers through strategies such as heteroatom interface creation [10], defect engineering [11] and heteroatom doping [12], there is still a lack of studies on crystal surface modulation. It has been reported that the engineering of crystal facets can modulate thermal [13,14], photocatalytic [15] and electrocatalytic [16,17] properties. Yin et al. [18] investigated the relationship between Fe_2O_3 facets and H_2O_2 activation efficiency, and found that Fe_2O_3(311) had the lowest adsorption energy and H_2O_2 activation energy barrier, and exhibited good H_2O_2 activation efficiency. Gu et al. [19]. found a significant crystallographic plane dependence of hematite-catalysed phthalate hydrolysis, related to the atomic arrangement of surface-uncoordinated Fe.

In addition, Hematite exhibits a variety of exposed crystal surfaces [20], and the exposed crystal surface of Fe-based oxygen carriers changes during redox cycling [21]. Nevertheless, most of the reaction mechanisms of Fe-based oxygen carriers focus on single crystal faces [22–24]. The correlation between Fe_2O_3 crystal faces and CH_4-CLC performance, and a molecular level explanation of the reaction mechanism remain lacking. Therefore, it is a valuable work to elucidate the contribution of Fe_2O_3 from different crystal faces to CH_4-CLC performance, taking into account the different coordination abilities of different crystal faces.

In this work, we systematically investigate the influence of Fe_2O_3 crystal facet effects on the mechanism of methane oxidation during chemical looping reactions. Firstly, a series of Fe_2O_3 oxygen carriers with different exposed crystalline surfaces (Fe_2O_3(001), Fe_2O_3(012) and Fe_2O_3(104)) were synthesized, characterized and tested. Then, the differences in physicochemical properties and redox activity are explained in conjunction with detailed characterization analysis and coupled electronic structure properties. Finally, the effects of the exposed crystalline surfaces on oxygen migration and microscopic surface reaction mechanisms were revealed in combination with reactive force field simulations and density functional theory calculations. These findings enhance our understanding of the microscopic mechanisms of action of Fe-based oxygen carriers and provide novel methodologies for designing oxygen carriers used in the chemical looping process.

2. Experimental and computational details

2.1. Synthesis of Fe-based oxygen carriers

Three types of α-Fe_2O_3 nanocrystals oxygen carriers (OCs) with different exposed crystal faces were synthesized by hydrothermal method [22,25,26]. For α-Fe_2O_3 (001)(HNP), $FeCl_3$ $6H_2O$ (0.54 g) and CH_3COONa (2 g) were dissolved in 30.0 mL ethanol with a trace addition of 1.0 mL deionized water, then the mixture was sealed in a Teflon-lined autoclave and maintained at 180 °C for 12 h. For α-Fe_2O_3 (104)(HNR), 1.10 g $FeCl_3{\cdot}6H_2O$ and 1.21 g urea were dissolved in 40 mL of distilled water, and then 1.65 g formamide ($HCONH_2$) was added. The mixture was sealed in a Teflon-lined autoclave and maintained at 120 °C for 12 h. For α-Fe_2O_3 (012)(HNC), dissolve $FeCl_3$ $6H_2O$ (1.0 mmol) in 10 mL ethanol and add 2.5 mL deionized water, add 0.8 g sodium acetate and allow to dissolve completely, then maintain the suspension at 180 °C for 12 h in a Teflon-lined autoclave. The product was collected by centrifugation and washed at least 5 times alternately with water and ethanol, then dried at 60 °C for 10 h and calcined at 500 °C for 5 h.

2.2. Oxygen carrier characterization

X-ray diffraction (XRD) was performed on an X'pert Pro diffractometer (PANalytical Company) utilising Co Kα as the radiation source across a range of 10–90° with a scan speed of 8°/min. The microstructural characterization was performed using on a transmission electron microscope (JEM-F200) equipped with an energy dispersive X-ray spectrometer (EDS) operating at 200 kV. Hydrogen programmed temperature rise reduction (H_2-TPR) by chemisorption was performed by pretreating 30 mg of the sample in a stream of He at 300 °C for 1 h, then cooling to 50 °C. The sample was then heated to 900 °C in a stream of 10 vol% H_2/He at a ramp rate of 10 °C/min. The X-ray photoelectron spectroscopy (XPS) tests were performed using a spectrometer (PHI-1600 ESCA). The characteristic binding energy (BE) peak of C 1s (284.80 eV) was used to calibrate the binding energy (BE) values. The nitrogen adsorption and desorption isotherms were measured using a Micromeritics 3Flex instrument. Prior to the measurement, the samples were degassed under vacuum at 150 °C for 12 h.

2.3. Chemical looping combustion (CLC) experiments

Activity tests were evaluated during the chemical looping process using a fixed-bed piston flow reactor (18 mm inner diameter). 200 mg of sample held in place by quartz wool were placed in the tubular reactor, then heated to 300 °C under N_2 stream (100 mL/min). Following a 5-minute purging period, the sample was heated further to 800 °C. When the desired temperature was reached, the gas flow was stopped and N_2 was introduced at the same flow rate and held for 5 min, then switched to the reaction gas (5% CH_4/N_2 100 mL/min). The exhaust gas was collected in a gas bag through a condensation unit for analysis by gas chromatography (An Agilent 7890B) equipped with a thermal conductivity detector (TCD) and a Porpak Q packed column (Alltech). The methane conversion and CO_2 selectivity were determined as follows.

$$CH_4\text{conversion} = \frac{moles\ of\ CH_4\ consumed}{moles\ of\ CH_4\ introduced} \times \mathbf{100}\% \quad (1)$$

$$CO_2\text{selectivity} = \frac{moles\ of\ CO_2\ consumed}{moles\ of\ CH_4\ introduced} \times 100\% \quad (2)$$

2.4. Density functional theory (DFT) details

All calculations were performed using the CP2K code [27]. The exchange energy was described using the Perdew-Burke-Ernzerhof spin--polarized generalized gradient approximation [28]. The wave function was described using the Goedecker-Teter-Hutter pseudopotential and a double-zeta basis set with a cutoff energy of 500 Ry. The DFT + U was utilized with Hubbard corrected U value of 4.0 eV for Fe [29]. The Brillouin zone using gamma point. DFT-D3 scheme with an empirical damping potential term were added [30]. The configurations were optimised using the Bloeden-Fletcher-Goldfarb-Sanno (BFGS) algorithm until all the forces were less than 4.5×10^{-4} Hartree/Bohr. The transition states of primitive reactions were identified through CI-NEB [31] as well as the dimer algorithm [32]. All transition states are identified with only a single imaginary frequency. Gibbs energy was calculated at 1073.15 K.

The lattice optimization of Fe_2O_3 resulted in calculated lattice parameters of a = b = 5.04 Å and c = 13.86 Å. These values are in good agreement with the experimental (a = b = 5.04 Å and c = 13.77 Å) and theoretical (a = b = 5.04 Å and c = 13.87 Å) values [33–35]. A 15 Å vacuum gap is left on the surface to eliminate unphysical interactions between the periodic systems. The crystal cell is set to be antiferromagnetic. The supercell models adopted for each crystal surface are shown in Fig. S1. All the visualizations were produced by the VESTA [36].

2.5. Molecular dynamics (MD) simulation

ReaxFF MD simulations were performed using the ReaxFF code [37] implemented in the Large Scale Atomic/Molecular Massively Parallel Processor Simulator (LAMMPS) package [38]. Molecular dynamics simulations based on the Fe/C/H/O force field [39] in the time range of 250–1000 ps were performed using the NVT system to study CH_4 on Fe_2O_3 from 1000 to 3000 K. The temperature is increased artificially in order to accelerate the reaction, which has been widely used in previous studies [40,41]. Before running the MD simulations, each system was first subjected to energy minimization using a conjugate gradient algorithm and a 20,000-step non-reaction relaxation process at 300 K to bring it to the ground state to eliminate possible simulation artefacts due to the initial high-energy contact. In the MD simulations, the step size was 0.25 fs, the temperature was controlled by Nosé-Hoover, and the damping constant was 0.1 ps. The period box for the ReaxFF MD simulations was 100 Å × 100 Å × 50 Å, and the constructed Fe-based oxygen carrier with methane model is shown in Fig. S2. The Fe_2O_3 crystal surface model was obtained by DFT pre-optimization as described in section 2.4.

3. Results and discussion

3.1. Structure and morphology

The XRD patterns of α-Fe_2O_3 samples synthesized by different methods are shown in Fig. 1(a). All of them show the standard hematite phase (according to the standard JCPDS 33–0664) [42]. The diffraction peaks are strong and sharp, indicating that the three samples are well crystallised and and do not contain other crystalline impurities. For α-Fe_2O_3(001), the 104 peak becomes weaker while the 110 peak remains higher, suggesting that the crystals are better developed in the c-direction, i.e., the main exposed crystal face is (001). As illustrated in Fig. 1(b), the N_2 adsorption-desorption isotherm for all samples is presented. In accordance with the IUPAC classification, all oxygen carriers are observed to exhibit type IV isotherms, accompanied by characteristic H3 hysteresis loops. This suggests that the materials possess mesoporous properties. The surface areas of Fe_2O_3(001), Fe_2O_3(012), and Fe_2O_3(104) are 5.13, 2.42, and 3.00 m^2/g, respectively (see Supplementary materials Table S1). It is evident that there is negligible variation in the surface areas of the three oxygen carriers, with only the specific surface area of Fe_2O_3(001) exhibiting a slight increase.

Scanning electron microscopy (SEM) and high-resolution transmission electron microscopy (HRTEM) were used to characterize the morphology and crystal structure of the three classes of OCs, as shown in Fig. 2. The HNPs particles are in the shape of uniform hexagonal plates with side lengths of 90–120 nm and thicknesses in the range of 26–28 nm. The HR-TEM images and FFT patterns clearly show that the lattice spacing on HNPs is 0.25 nm, which corresponds to the Fe_2O_3(001) facets. The HNC particles show a regular pseudo-cuboidal shape with their average side lengths of about 200 nm. Careful observation of the HR-TEM images and FFT patterns shows that the lattice spacing of the HNC particles is 0.37 nm, which is attributed to the Fe_2O_3(012) facets. The HNR particles have a regular prismatic shape, and their lattice edge lengths are in the range of 30–60 nm, with a lattice spacing of 0.27 nm. The HNR particles have a regular lattice spacing of 0.27 nm, which is consistent with the spacing of the Fe_2O_3(104) facets. In addition, the material composition of the synthesized particles was verified using energy spectroscopy. Fig. 3 clearly shows the HAADF image as well as the EDS mapping spectrum of the synthesized oxygen carrier. This shows the presence of Fe and O in the synthetic oxygen carrier with uniform distribution.

3.2. Performance of oxygen carriers

In order to reveal the differences in reactivity due to the exposure of the crystalline surfaces, successive redox cycling reactions were carried out on three Fe_2O_3 oxygen carriers. The conversion of CH_4 and the selectivity of CO_2 as evaluation indicators. Fig. 4 shows the redox

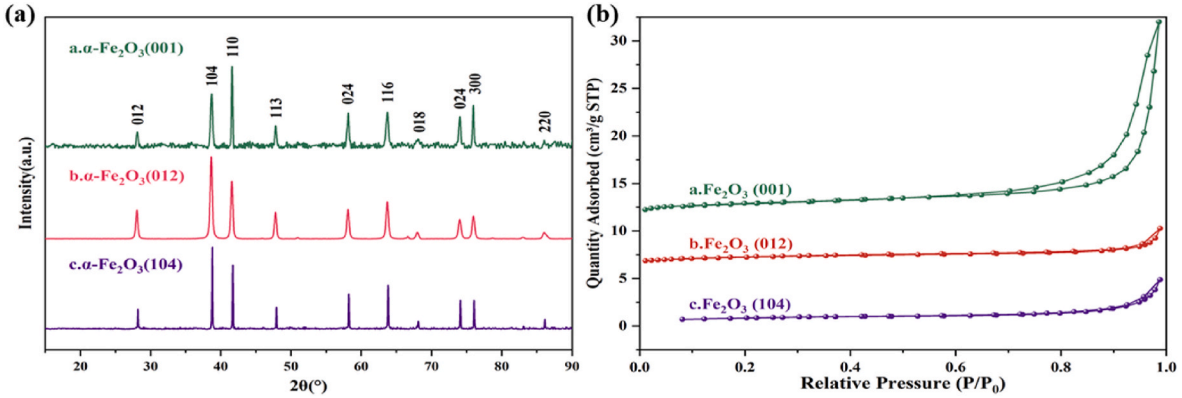

Fig. 1. The powder X-ray diffraction (XRD) patterns of (a) HNP, (b) HNC, and (c) HNR (104).

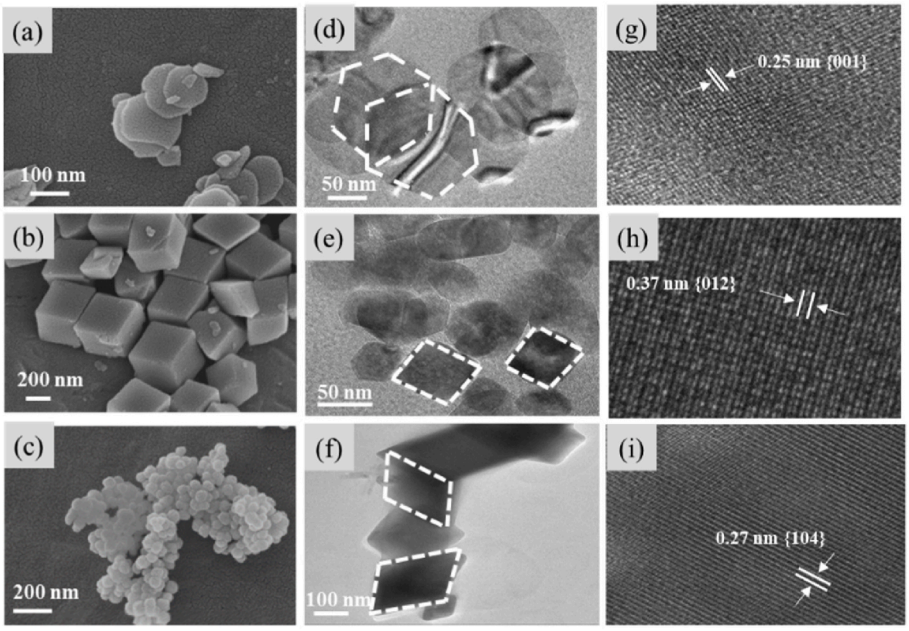

Fig. 2. (a–c) SEM images, (d–i) HRTEM images; SEM and HRTEM images of hematite nanoplate (HNP) (a, d, g), hematite nano-cube (HNC) (b, e, h), and hematite nano-rhombohedra (HNR) (c, f, i).

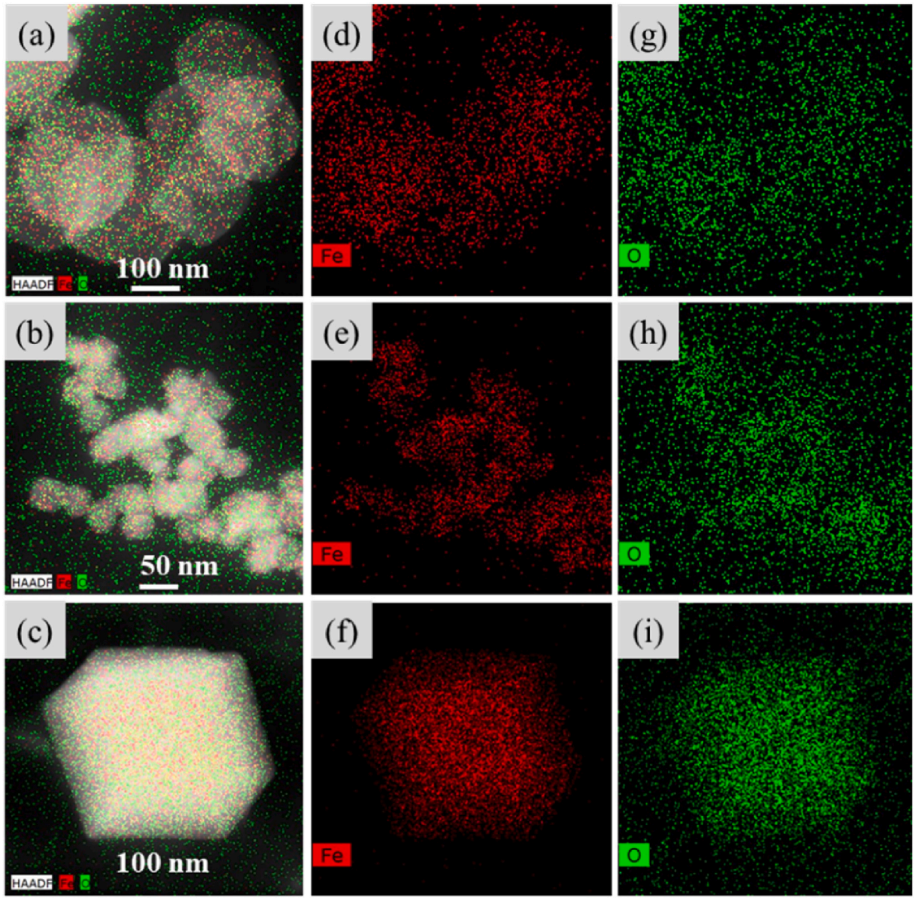

Fig. 3. HAADF-STEM images and EDS elemental mapping images of hematite nanoplate (HNP) (a, d, g), hematite nano-cube (HNC) (b, e, h), and hematite nano-rhombohedra (HNR) (c, f, i).

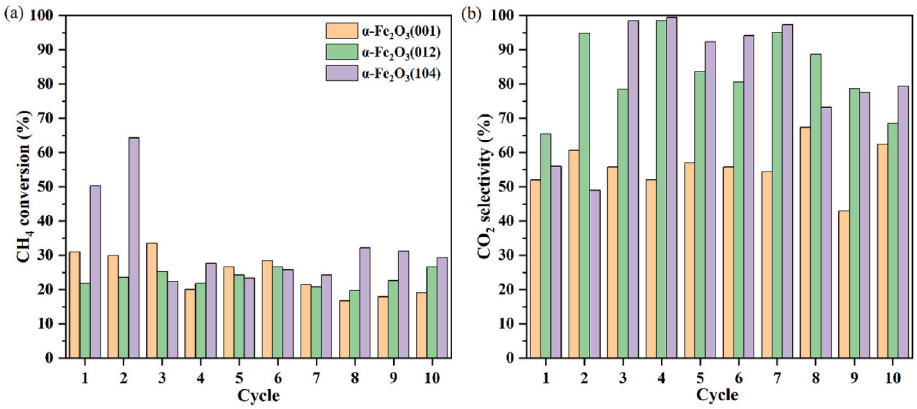

Fig. 4. Activity test of the oxygen carriers at 800 °C: (a) CH_4 conversion and (b) CO_2 selectivity.

performance of the three Fe_2O_3 samples for 10 consecutive cycles. As shown in Fig. 4(a), it is observed that the order of CH_4 conversion is $Fe_2O_3(104) > Fe_2O_3(012) > Fe_2O_3(001)$. $Fe_2O_3(104)$ exceeds that of the other two samples. In the initial two cycles, the CH_4 conversion of $Fe_2O_3(104)$ exhibited a marked increase compared to the other two samples, reaching up to 64 %. However, as the number of cycles increased, the CH_4 conversion gradually decreased. After 10 cycles, the conversion was reduced to 31 %. This deactivation may be associated with structural damage caused during repeated cycling(Fig. S3). A similar deactivation phenomenon is shown on the crystalline surfaces of both $Fe_2O_3(001)$ and $Fe_2O_3(012)$, which is consistent with the susceptibility of pure Fe_2O_3 to deactivation derived from the work of Ma et al. [43]. Fig. 4(b) shows the CO_2 selectivity of the three samples. It is evident that the CO_2 selectivity of $Fe_2O_3(012)$ and $Fe_2O_3(104)$ can attain 100 % after two activation cycles, while the CO_2 selectivity of $Fe_2O_3(001)$ is approximately 60 %, which is considerably lower than the other two samples. This suggests that $Fe_2O_3(104)$ and $Fe_2O_3(012)$ have sufficient reactive lattice oxygen to provide it to the methane and reaction products to achieve complete combustion of the methane. The above results indicate that $Fe_2O_3(104)$ combines superior CH_4 reactivity with CO_2 selectivity.

3.3. Reducibility behaviour

To further illustrate the reduction behavior of α-Fe_2O_3 arising from differences in the exposed crystal surfaces, H_2-TPR tests were performed on all the oxygen carriers and different reduction behaviors were observed, as shown as in Fig. 5. All H_2-TPR profiles can be divided into two distinct regions, a sharp reduction peak in the low temperature region (300–400 °C), and a broad peak in the high temperature region (450–800 °C). The former reflects the reduction of Fe_2O_3 to Fe_3O_4 due to oxidation of the surface lattice oxygen. The latter reflects the reduction of magnetite to ferrous iron oxide and then further to metallic iron. The former reflects the reduction of Fe_2O_3 to Fe_3O_4 due to oxidation of surface lattice oxygen, and the latter reflects the reduction of Fe_3O_4 ($Fe_3O_4 \rightarrow$ FeO → α-Fe) due to oxidation of bulk phase lattice oxygen. In general, the conversion of Fe_2O_3 to Fe_3O_4 allows the complete oxidation of CH_4, and the conversion of Fe_3O_4 to Fe is accompanied by the partial oxidation of CH_4 [44]. Therefore, a lower reduction temperature in the low-temperature region indicates easier lattice oxygen removal and greater reactivity of the oxidized CH_4. Therefore, the low temperature reduction temperatures of the three are, in order, $Fe_2O_3(104) > Fe_2O_3(012) > Fe_2O_3(001)$. This result is consistent with the order of magnitude of the oxygen vacancy formation energy and the lattice oxygen migration energy, as obtained from subsequent DFT calculations (Fig. 10). This result is consistent with the order of magnitude of the oxygen vacancy formation energies obtained from the subsequent DFT calculations. For $Fe_2O_3(001)$, $Fe_2O_3(012)$, and $Fe_2O_3(104)$, the hydrogen consumption from the surface reduction peak area was 0.60 mmol/g, 0.99 mmol/g and 1.04 mmol/g, respectively(Table S2). This demonstrates that $Fe_2O_3(104)$ has a higher surface lattice oxygen reactivity.

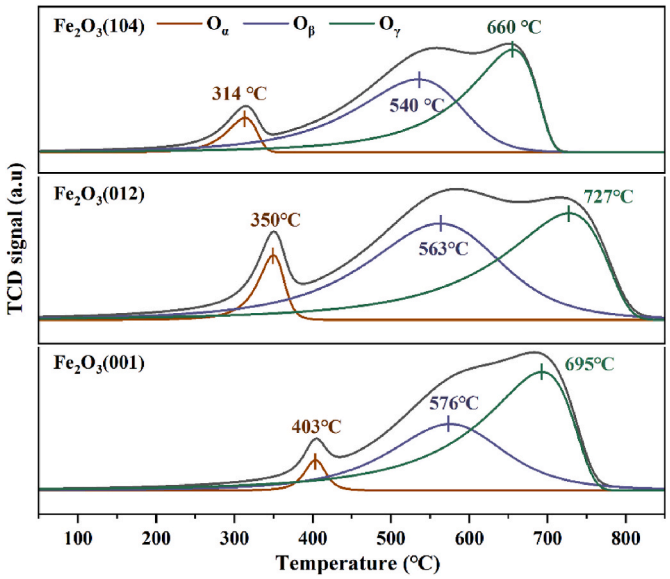

Fig. 5. H_2-TPR profiles of three samples.

3.4. Chemical states and surface oxygen vacancies

The surface composition and chemical state of prepared oxygen carriers were investigated by XPS, and the detailed analysis results were displayed in Fig. 6. Fig. 6(a) shows the high resolution XPS spectrum of Fe 2p. It can be seen that Fe 2p has two typical strong peaks at ~724.4 and ~710.9 eV, which are attributed to the spin orbitals Fe 2p 1/2 and Fe 2p 3/2, respectively [45,46]. The main peaks of Fe 2p 3/2 are characteristically fitted to Fe^{3+} (~712.9 and ~710.8 eV) and Fe^{2+} (~709.6 eV). Besides, two satellite peaks are clearly distinguishable at ~718.3 and ~732.8 eV. The presence of low-valence Fe^{2+} indicates a partial reduction of Fe^{3+}, accompanied by the presence of oxygen vacancies(OVs) to maintain electrostatic balance. A lower ratio of Fe^{3+}/Fe^{2+} means the higher content of OVs as the active sites in the oxidation process, as shown as in Fig. 6(c).

The O 1s spectrum in Fig. 6(b) can be decomposed into three distinct peaks at 531.9, 530.6 and 529.4 eV, which are attributed to surface hydroxyl or carbonate oxygen($O_{ads, OH}$), oxygen species chemisorbed at OVs over oxygen carriers (O_{ads}), and bulk lattice oxygen(O_{latt}), respectively [47]. In general, O_{ads} were considered to be reactive oxygen

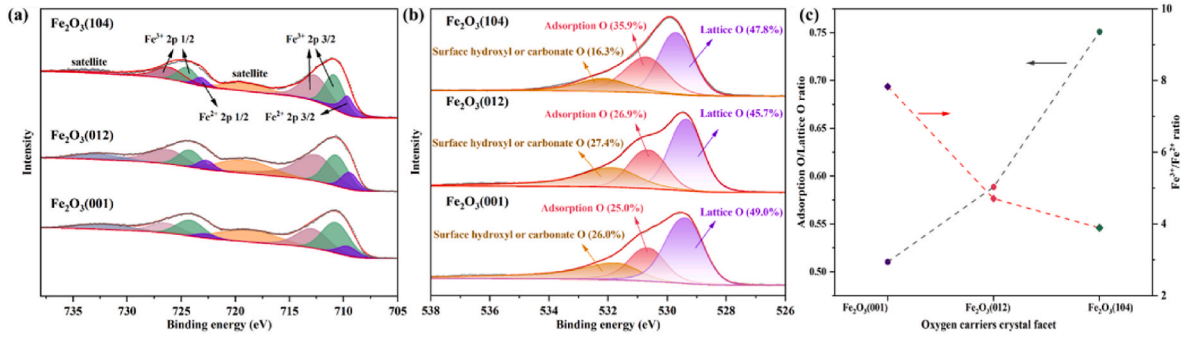

Fig. 6. XPS spectra of three α-Fe_2O_3 samples of (a) Fe 2p, (b) O 1s and (c) Plotting adsorption O/lattice O ratio obtain from the O 1s XPS versus three α-Fe_2O_3 samples.

species with higher activity than bulk lattice oxygen [48]. Consequently, the ratio O_{ads}/O_{latt} can be employed as a descriptor to characterize the activity of the lattice oxygen of the oxygen carriers. A higher O_{ads}/O_{latt} ratio is indicative of elevated oxygen activity. As illustrated in Fig. 6(c), the ratio of O_{ads}/O_{latt} increases with facet index, indicating that the higest amount of OV is located on the surface of oxygen carriers with high exposure index facets. This is consistent with the low Fe^{3+}/Fe^{2+} ratio and the weaker bonding energy of Fe(II)–O compared with Fe(III)–O, which favours oxygen release. Furthermore, for Fe_2O_3 (104), it can be observed that the peaks of the oxygen species spectra are shifted in the direction of increasing binding energy as the oxygen vacancy concentration increases. It can be posited that a substantial concentration of oxygen vacancies results in electron remolecularisation and the loss of electrons by O atoms. This hypothesis is further substantiated by the upward shift of the centre of the O-2p band of Fe_2O_3 (104) (Fig. 12). In conclusion, the order of the lattice oxygen activity of the oxygen carriers is as follows: $Fe_2O_3(104) > Fe_2O_3(012) > Fe_2O_3(001)$. In summary, the differences in the CH_4 oxidation activity of the different crystal facet oxygen carriers appear to be due to the oxygen activity caused by the oxygen vacancy content on the surface of the oxygen carriers.

3.5. Molecular dynamics(MD) analysis

Based on the demonstration of the influence of crystal surface on CH_4 oxidation activity and surface oxidation environment, reactive force field molecular dynamics (Reaxff-MD) simulations were performed to reproduce the dynamic characteristics of the CH_4 oxidation process on oxygen carrier.

MD simulations of the reaction process of the Fe_2O_3–CH_4 system of the CLC process have been investigated at temperatures of 1000, 1273, 1600, 2000 and 3000 K, respectively. The effect of reaction temperature on the potential energy of the system is shown in Fig. S4, from which it can be seen that the potential energy decreases to a minimum at 200 ps and remains stable, indicating that the CH_4 oxidation system has reached reaction equilibrium. Fig. S5 shows the variation of the number of CH_4 with Fe_2O_3 at different temperatures. It can be seen that the higher the temperature, the more the number of CH_4 oxidations decreases within 200 ps. At 1273 K, the number of CH_4 shows a significant decrease, while at 3000 K the number of CH_4 is depleted at about 150 ps. Therefore, a comparative analysis of the evolution of CH_4 and reaction products at each temperature allows the dynamic nature of the overall CH_4 reaction process to be elucidated.

Fig. 7(a) gives mean square displacement (MSD) of CH_4 on different Fe_2O_3 surfaces. It is clear that the order of the MSD slopes follows $Fe_2O_3(104) > Fe_2O_3(012) > Fe_2O_3(001)$ over all range of time scale. This implies that CH_4 has a faster diffusion rate on high exposure index crystalline surfaces. In other words, CH_4 is adsorbed faster on $Fe_2O_3(104)$, with a kinetic adsorption advantage. This can also be explained in terms of the radial distribution function (RDF). Fig. 7(b) shows the radial distribution function of CH_4 as an oxygen carrier at different exposed crystal surfaces. It is clear that the g(r) values follow the order: $Fe_2O_3(104) > Fe_2O_3(012) > Fe_2O_3(001)$, confirming a stronger interaction between CH_4 and $Fe_2O_3(104)$. The radial distribution function between Fe–O is given in Fig. 7(c) to give an idea of the distribution between the oxygen carrier atoms. The radial distribution peak at 1.95 Å is attributed to the Fe–O bond, and the remaining peaks can be attributed to oxygen released from the Fe bond, originating from reaction intermediates or reaction products. This reflects the oxygen supply capacity of the oxygen carriers, and the $Fe_2O_3(104)$ crystal surface clearly has a better ability to oxidize CH_4. This is in agreement with our experimental tests (Fig. 4). It confirms the validity of the molecular dynamics simulation results.

Fig. 8 illustrates the variation in the number of species within the reaction system over time at different temperatures. It is evident that the quantity of CH_4 diminishes rapidly at the onset of the reaction, subsequently decelerating in all the reaction systems. The alteration in the number of CH_4 can be used to a certain extent to characterize the extent of the reaction. That is to say, CH_4 reacts rapidly at the commencement

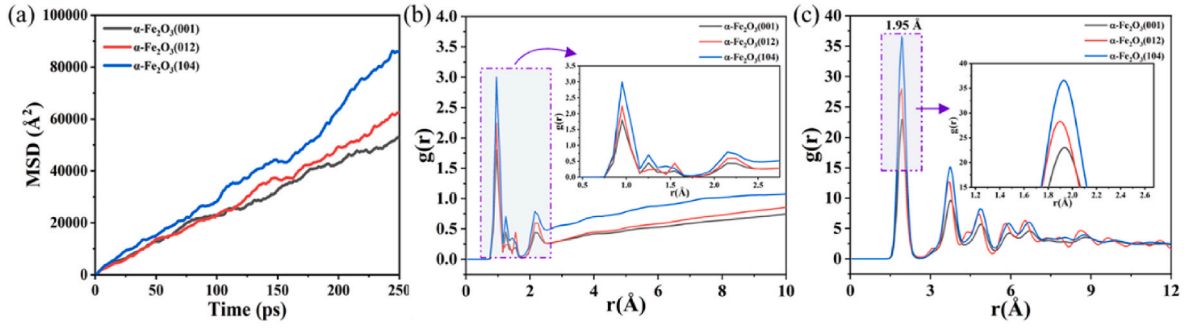

Fig. 7. (a) Mean square displacement of CH_4 on different facet,(b) Radial distribution function curve of CH_4 with different facet,(c) Radial distribution function curve of Fe–O in different facet.

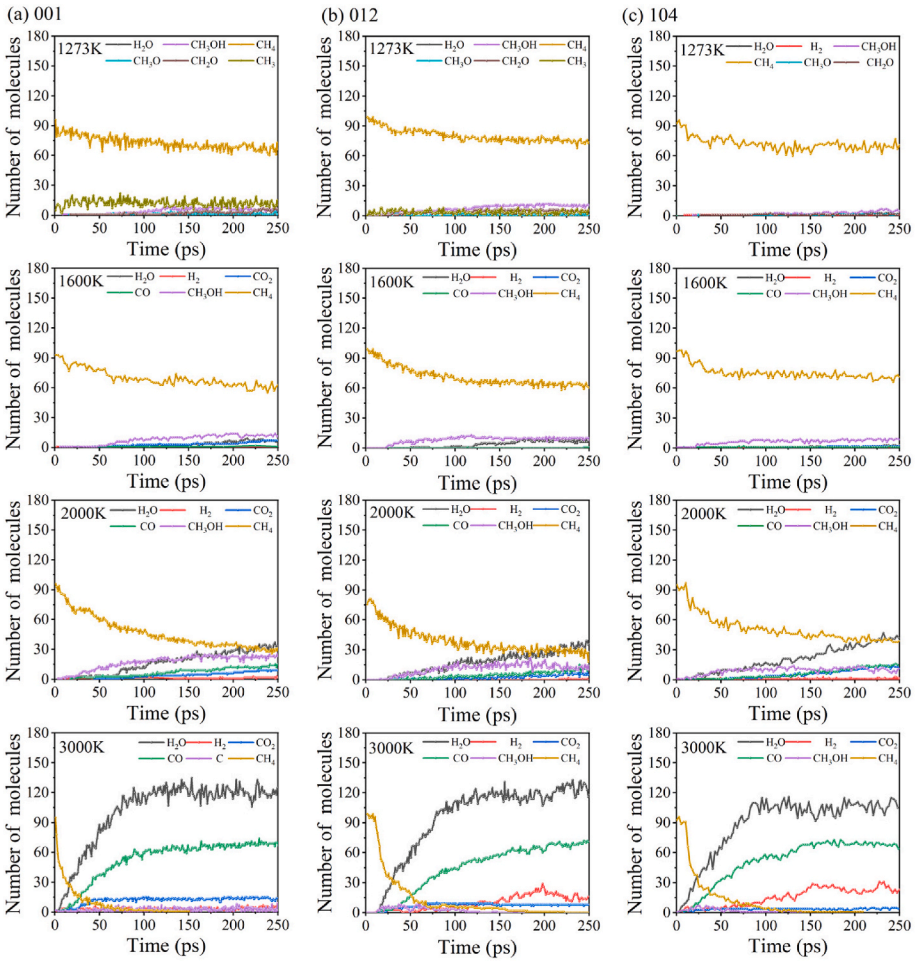

Fig. 8. Number of changes in major intermediates/products (five common species) during CH_4 oxidation on the surface of (a)Fe_2O_3(001), (b)Fe_2O_3(012), (c)Fe_2O_3(104).

of the reaction and slows down thereafter, which is consistent with the thermogravimetric results of Monazam et al. [49]. This also briefly confirms the reasonableness of the MD simulation. At 1273 K, it was observed that the generation of CH_3 occurred first on both Fe_2O_3(001) and Fe_2O_3 (012) following CH_4 cleavage, and that the former exhibited a higher number of CH_3 than the latter. This suggests that the cleavage of CH_4 is the initial step in the formation of CH_3, and that CH_4 cleavage is more thermodynamically favorable on Fe_2O_3(001), which is consistent with the H_2-TPR(Fig. 5) and DFT results(Fig. 11). As the reaction progresses to approximately 75 ps, the formation of CH_3OH becomes evident. This is due to the fact that the hydrogen atom formed by cleavage hydroxylates oxygen. CH_3OH reacts readily with the hydroxyl group to form CH_3OH [23]. At approximately 100 ps, the formation of CH_3O and CH_2O is observed, albeit in negligible quantities. It is reasonable to hypothesise that CH_3OH continues to cleave to form CH_3O and CH_2O. For Fe_2O_3(104), the formation of predominantly CH_3OH, CH_3O and CH_2O is clearly visible. These intermediates are consistent with our previous observation of methane reaction intermediates in polycrystalline iron oxide particles using in situ spectroscopy [50]. Fig. 9 summarizes the reaction history of CH_4 oxidation on different crystalline surfaces. The oxidation pathways of CH_4 are essentially similar on different facet.

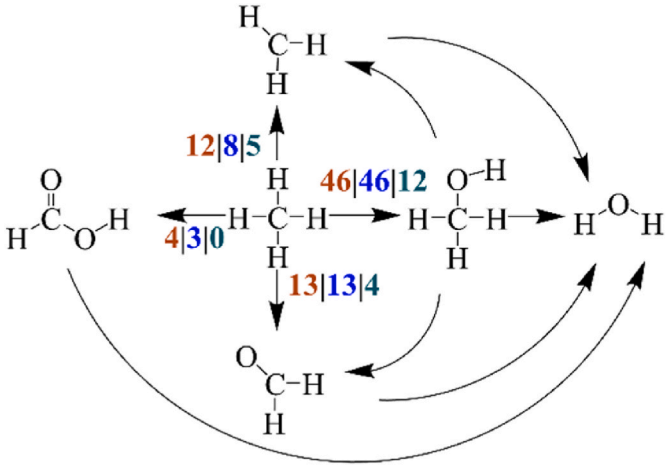

Fig. 9. Main oxidation pathways of methane on Fe_2O_3 surface (Numbers indicate frequency of response, brown:001, blue:012,dark cyan:104). (For interpretation of the references to color in this figure legend, the reader is referred to the Web version of this article.)

At 1600 and 2000 K, accompanied by a tendency for CH_3OH to increase and then decrease slightly, H_2O begins to increase rapidly. The production of H_2 is exclusively observed at 2000 K, thereby indicating that the formation of H_2O is deemed to be more thermodynamically favorable. MD simulations also predicted the production of carbon dioxide and carbon monoxide molecules. There was a gradual increase in CO and CO_2 at 2000 K. At 3000 K, CH_4 is depleted in about 75 ps. A rapid increase in the number of CO and H_2O is observed during the process. This suggests that high temperatures favour the formation of

CO. It is worth noting that after the consumption of CH_4, CO_2 remains at a certain number while CO continues to increase. It can be deduced from the evidence presented that the disparity in the exposed crystalline surfaces of Fe_2O_3 results in the more efficient formation of the by-product CO at elevated temperatures. In addition, H_2 is also rapidly produced for Fe_2O_3(012) and Fe_2O_3(104). This may be due to the reduction of H_2O to H_2, as documented in the literature, Fe_3O_4 and FeO have the potential to reduce H_2O to H_2 [51]. Another fact is that the increase in the number of H_2 is accompanied by a decrease in the number of H_2O. In other words, the facet effect of Fe_2O_3 leads to differences in the reduction of H_2O.The production of C can be observed at Fe_2O_3(001). From the fact that the amount of C remains in a certain ratio to H_2, it can be inferred that it is the direct cleavage of CH_4 by Fe activation to form C + H_2. And it can be seen that the number ratio of H_2O to CO after the reaction has stabilized in the stoichiometric ratio, which further confirms that the oxidation of C requires a high temperature to overcome the activation energy barrier. The RDF distribution of Fe–O bonds shown in Fig. 7(c) also indicates that the amount of Fe–O bonds in Fe_2O_3(001) is low during the reaction, which supports the above speculation. Comparing the number of CO_2 and CO at different temperatures, the number of CO_2 decreases and the number of CO product molecules increases as the reaction progresses, which may be related to the fact that CO_2 continues to react with C to form CO at high temperatures.

3.6. DFT analysis reaction mechanism

3.6.1. Oxygen supply mechanism

The formation of oxygen vacancies and the ease of oxygen migration are analyzed based on DFT calculations to elucidate the relationship between lattice oxygen and crystal surface activity. The oxygen vacancy formation energy (Ev) is defined as follows:

$$E_V = E_{defect} - E_{perfect} + 1/2O_2 \quad (3)$$

Where the E_{defect} and $E_{perfect}$ present the energy of structure with oxygen vacancies and without oxygen vacancies respectively, and the E_{O2} denotes the energy of the free oxygen atom.

As shown in Fig. 10(a), the oxygen vacancy formation energies of Fe_2O_3(001), Fe_2O_3(012) and Fe_2O_3(104) are 6.17, 2.16 and 2.03 eV, respectively. The larger the oxygen vacancy formation energy, the more difficult it is to lose oxygen. Obviously, the Fe–O bond strength of the high index exposed crystal surface gradually decreases the easier it is to form oxygen vacancies. In other words, they become progressively more reducing. This is consistent with our experimental results(Fig. 5). The decrease in oxygen vacancy formation energy increases the reactivity of the oxygen carrier and promotes the rapid CLC reaction. To further investigate the oxygen supply capacity of Fe_2O_3, the migration of oxygen atoms within the Fe_2O_3 system was examined. As illustrated in Fig. 10 (b), the vertical migration of oxygen atoms was considered in the presence of oxygen vacancies on the surface. The activation energy barriers for the migration of Fe_2O_3(001), Fe_2O_3(012) and Fe_2O_3(104) are 1.25, 1.15 and 0.46 eV, respectively. This indicates that it becomes increasingly facile for oxygen atoms in the subsurface layer to occupy surface oxygen vacancies. In summary, the results of the DFT calculations indicate that Fe_2O_3(104) is advantageous in providing both surface

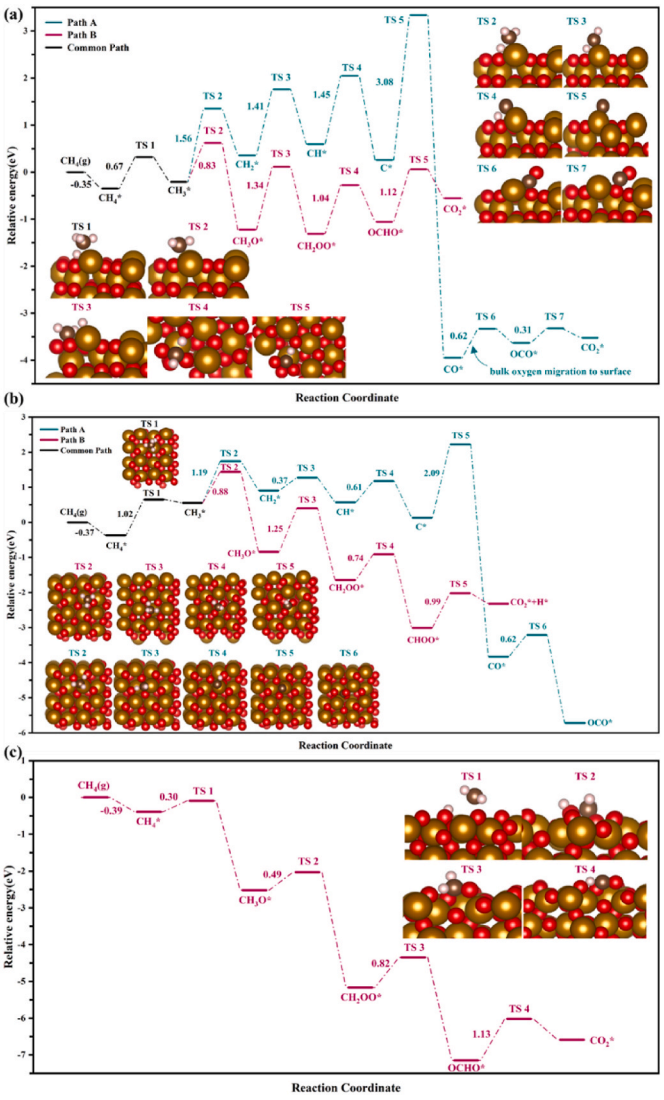

Fig. 11. Reaction energy diagram of the CH_4 oxidation on (a) Fe_2O_3(001), (b) Fe_2O_3(012), (c)Fe_2O_3(104).

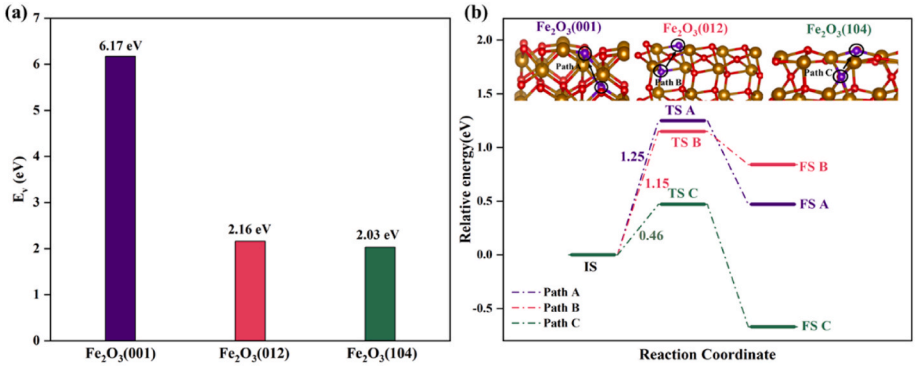

Fig. 10. (a) Oxygen vacancy formation energies and (b) Oxygen transfer pathways.

lattice oxygen and bulk phase oxygen migration to provide surface lattice oxygen.

3.6.2. Surface reaction mechanism

To further elucidate the relationship between the bare crystalline surface of iron oxide and the CH_4 reaction properties, we performed DFT calculations based on MD trajectory analyses to obtain the detailed surface reaction mechanism and kinetic details during the CH_4 oxidation process.

It is generally accepted that methane oxidation goes through a series of basic steps, including methane adsorption, C–H bond cleavage and lattice oxygen oxidation (including C/O and H/O recombination). Therefore, the adsorption process of CH_4 as well as the reaction intermediates (Fig S6, S7 and S8) on different crystal planes of Fe_2O_3 was considered first. The results(Table S3, Table S4, and S5) demonstrated that CH_4 exhibited a tendency to adsorb at the Fe site of Fe_2O_3(001), the 5-coordinated Fe site of Fe_2O_3(012) and the O3c site of Fe_2O_3(104). The surface reaction processes of adsorbed CH_4 were then studied, as shown as in Fig. 11.

We have previously elucidated the oxidation mechanism of CH_4 on the surface of Fe_2O_3(001) through experiments and DFT calculations. Fig. 11 (a) shows the oxidation mechanism of CH_4 on Fe_2O_3(001) [50]. In path A, the cleavage of CH_4 takes place at the Fe site. CH_4 is first adsorbed at the Fe site. And then sequentially cleaved to form CH_3*, CH_2*, CH*, and C*, requiring activation energy barriers of 1.56, 1.41 and 1.45 eV respectively. The hydrogen removed by the cleavage is transferred to the O site attached to Fe to form OH*. The C* that is formed by the cleavage is oxidized by the lattice oxygen to form CO*. It is worth noting that the activation barrier to be overcome for this reaction is as high as 3.08 eV, and the exothermic energy is 4.02 eV. CO* reacts readily with lattice oxygen to form CO_2. The process consists of a two-step reaction. The oxidation pathway of CH_4 at the O site was also considered, as shown in path B. CH_4 on the Fe site results in the dehydrogenation of the molecule, forming methoxy (OCH_3*). The subsequent adsorption of CH_3* on the Fe site overcomes an activation energy barrier of 0.83 eV, enabling the transfer of the molecule to O site. The sequential dehydrogenation of OCH_3* to form CH_2OO* and HCOO* is a process that requires activation energy barriers of 1.34 and 1.04 eV, respectively. Eventually, HCOO* is dehydrogenated through the activation of the C–O bond, resulting in the formation of CO_2* and desorption to form CO_2.

Fig. 11 (b) shows the oxidation mechanism of CH_4 on Fe_2O_3(012). The CH_3* formed by the dehydrogenation of the CH_4 activated at the Fe site was adsorbed at the Fe site and the H was transferred to the O site. Subsequent dehydrogenation and oxidation of CH_4 took place. Depending on the H-adsorbed O sites removed (O3c in the neighboring site and O3c in the inter-parallel site), two pathways exist. We found that H removed by CH_4* and CH_3* cleavage tends to adsorb on the inter-parallel O3c, and the activation energy barrier to be overcome is 1.02 and 1.19 eV, respectively. The H removed by CH_2*, CH* tends to adsorb on the neighboring O3c site, with an activation energy barrier to overcome of 0.37 and 0.61 eV, respectively. The C* is oxidized by lattice oxygen to form CO*, a process that overcomes an activation energy barrier of 2.09 eV. In a one-step oxidation reaction that overcomes an activation energy barrier of 0.62 eV, CO* is further oxidized by lattice oxygen to CO_2. In pathway B, CH_3* formed by dehydrogenation of CH_4 migrates from the Fe site to the neighboring O3c. Then a stepwise dehydrogenation overcomes 1.25, 0.74 eV to form CH_2OO* and HCOO*, respectively. Finally, the HCOO* overcomes 0.99 eV to form the CO_2*.

The mechanism by which CH_4 is oxidized in Fe_2O_3(104) is shown in Fig. 11(c). We found that CH_4 tends to adsorb at the O site. In addition, both Fe_2O_3(001) and Fe_2O_3(012) show superior pathways for the lattice oxygen reaction mechanism. Therefore, the oxidation pathway of CH_4 adsorbed at the Fe site is not considered in this study. The dehydrogenation of CH_4 adsorbed to the oxygen site to form CH_3* remains at the same site and H is transferred to the neighboring O site. The activation energy barrier for this process is 0.30 eV. Dehydrogenation of CH_3* tends to form the bidentate formate CH_2OO*, which is then dehydrogenated to form CHOO*, the former having to overcome an activation energy barrier of 0.49 eV and the latter having to overcome an activation energy barrier of 0.82 eV. CHOO* overcomes the activation energy barrier of 1.13 eV to form CO_2* together with dehydrogenation, and eventually desorbs to form CO_2.

From the above it can be seen that the lattice oxygen activation oxidation mechanism is not only a thermodynamically advantageous pathway compared to the Fe site activation pathway, but also avoids the formation of carbon accumulation by alkane cleavage. In addition, the difference in the arrangement of the surface atoms leads to significant differences in the detailed oxidation pathways as well as the activation energy barriers for CH_4. For Fe_2O_3(012) and Fe_2O_3(001), the rate-determining step(RDS) is $CH_3O^*+O_L \rightarrow CH_2OO^*+H$, and the activation energy barrier decreases from 1.34 eV for Fe_2O_3(001) to 1.25 eV for Fe_2O_3(012). $CHOO^* \rightarrow COO^*+H$ is the RDS for the Fe_2O_3(104), which has an activation energy barrier of 1.13 eV. Obviously, there is a crystal plane dependence of the CH_4 oxidation on Fe_2O_3 and α-Fe_2O_3(104) has a thermodynamic advantage.

3.6.3. Electronic structure characterization

In order to gain insight into the underlying physicochemical mechanisms by which crystal surface effects affect oxygen activity and key reactive processes, we have analyzed the electronic structure properties of key fundamental processes.

The partial density of states (PDOS) of the Fe_2O_3 are as shown in Fig. 12(a). In Fe_2O_3 oxygen carriers, the Fe-3d and O-2p orbitals are hybridized and show covalent bonding properties. At the Fermi energy level, the appearance of O-2p orbitals in Fe_2O_3(104) leads to a decrease in the band gap, an increase in the electron transfer capacity of Fe_2O_3(104). In addition, the top of the valence band of Fe_2O_3(104) is mainly contributed by O-2p orbitals, and its O-2p orbital peaks are stronger than those of other crystalline surfaces, indicating an enhanced O-electron donating capacity and increased lattice oxygen activity. This can also be described by the O-2p band center [48]. The O-2p band centers of Fe_2O_3(001), Fe_2O_3(012), Fe_2O_3(104) are −1.73 eV, −1.51 eV, −1.26 eV, respectively, which are gradually close to the Fermi energy level. This suggests that the change in the Fe–O coordination environment due to the crystal face effect effectively regulates the redox capacity of the lattice oxygen activated by O-2p.

The electronic-density-difference (EDS) before and after CH_3O adsorption are shown in Fig. 12(b). The yellow color in the EDS diagram represents an increase in charge and the indigo color represents a decrease in charge. It can clearly be seen that the charge of the C atom decreases significantly after CH_3 adsorption, while the charge on the O sites adsorbed by CH_3 accumulates. This indicates that electrons are transferred from CH_3 to O. According to the Lewis acid-base pair theory, CH_3 is the charge donor and is a Lewis base, while O is the charge acceptor and plays the role of a Lewis acid. Obviously, O, which is more capable of accepting charge, contributes to the charge transfer of the adsorbate and the bond between the two is stronger, thus contributing to the lowering of the activation energy barrier. As the density of states results show (Fig. 12(a)), the high index of O-2p exposing the crystal surface allows new occupied states at the valence tip, the empty states corresponding to the hole states created, implying that the O sites are able to accept more electrons. In other words, the O site becomes more Lewis acidic. Briefly, electronic structure characterization shows that high exposure of the crystalline surface results in enhanced interactions between the adsorb ate and the surface, which lowers the reaction activation energy barrier for the rate control step and facilitates the oxidation of CH_4.

4. Conclusion

Based on a series of combined experimental and theoretical

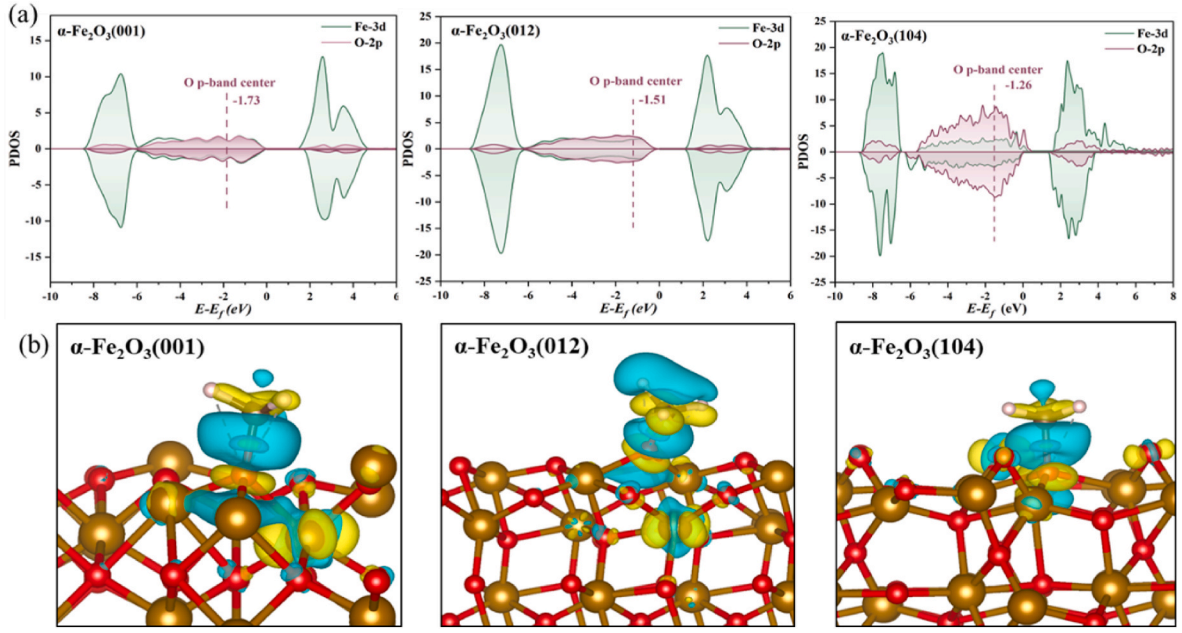

Fig. 12. (a) projected density of states of Fe_2O_3 oxygen carrier; (b) Isosurface plot of the difference in charge density due to CH_3* adsorption on the surface(yellow, charge accumulation; indigo, charge depleting; Isovalue: 0.005 electrons/Å^3). (For interpretation of the references to color in this figure legend, the reader is referred to the Web version of this article.)

measurements, this work investigates Fe_2O_3 facet-dependent (Fe_2O_3(001), Fe_2O_3(012), Fe_2O_3(104)) oxygen activity and reaction mechanism for CH_4 chemical looping combustion. The main conclusions can be drawn as follows.

(1) Compared with the (012) and (001) facets, Fe_2O_3(104) can effectively enhance the activity in CH_4 chemical looping combustion. This enhancement is attributed to an increase in the concentration of surface oxygen vacancies, an increase in the thermodynamic activity of lattice oxygen, and an increase in the rate of lattice oxygen donation and regeneration.
(2) CH_4 is dissociated and adsorbed on the surface to form OCH_3*, which are then sequentially dehydrogenated to form CH_2OO*, CHOO*, and finally CO_2 and H_2O are formed and desorbed. But the rate-controlling step transitions from OCH_3* dehydrogenation on Fe_2O_3(001)(E_a = 1.34 eV) and Fe_2O_3(012) (E_a = 1.25 eV) to CHOO* dehydrogenation on Fe_2O_3(104) (E_a = 1.13 eV)with progressively lower activation energy barriers.
(3) Exposure of crystalline surfaces perturbs the electronic structure of Fe_2O_3. The high exposure index of the crystalline surface leads to an upward shift of the valence band above the Fermi level and the creation of the O-2p vacancy state, which facilitates charge transfer from adsorbates. This process promotes C–H activation and lowers the activation energy barriers for the surface radical reactions.

In conclusion, this study proposes a methodology for the design of oxygen carriers with crystal surface engineering, with the aim of modulating the electronic structure. These findings will be of great assistance to researchers in the field of designing efficient oxygen carriers and reaction modulations.

CRediT authorship contribution statement

Junchang Xiong: Writing – original draft, Visualization, Investigation, Formal analysis, Data curation, Conceptualization. **Meirong Dong:** Writing – review & editing, Supervision, Resources, Project administration, Funding acquisition. **Zehua Huang:** Visualization, Validation, Investigation, Formal analysis, Data curation. **Hongchuan Liu:** Validation, Formal analysis. **Huaming Hou:** Resources. **Youcai Liang:** Supervision, Resources, Project administration. **Jidong Lu:** Supervision, Resources, Project administration.

Declaration of competing interest

The authors declare that they have no known competing financial interests or personal relationships that could have appeared to influence the work reported in this paper.

Acknowledgements

The research was supported by the National Natural Science Foundation of China (No. 52376107), and Foundation of Science and Technology Projects in Guangzhou (2025A04J7048). We also acknowledge the support from the Fundamental Research Funds for the Central Universities (2022ZFJH04) and Guangdong Province Key Laboratory of Efficient and Clean Energy Utilization (2013A061401005).

Appendix A. Supplementary data

Supplementary data to this article can be found online at https://doi.org/10.1016/j.ijhydene.2025.01.342.

References

[1] Krzywanski J, Ashraf WM, Czakiert T, Sosnowski M, Grabowska K, Zylka A, et al. CO_2 capture by Virgin Ivy Plants Growing up on the External Covers of Houses as a rapid Complementary Route to achieve global GHG reduction Targets. Energies 2022.
[2] National Academies of Sciences E, Medicine. Negative emissions technologies and reliable Sequestration: a research Agenda. Washington, DC: The National Academies Press; 2019.
[3] Jian Y, Tian M, He C, Xiong J, Jiang Z, Jin H, et al. Efficient propane low-temperature destruction by Co_3O_4 crystal facets engineering: Unveiling the decisive role of lattice and oxygen defects and surface acid-base pairs. Applied Catalysis B: Environmental. 2021;283:119657.
[4] Zhao Q, Hou X, Liu X, Chong M, Cheng D-g, Chen F, et al. Facet-dependent oxygen mobility and reaction pathways for oxidative dehydrogenation of 1-butene over Bi_2MoO_6. ACS Catal 2024;14:3543–55.

[5] Xin Y, Cheng L, Lv Y, Jia J, Han D, Zhang N, et al. Experimental and theoretical insight into the facet-dependent mechanisms of NO oxidation Catalyzed by structurally Diverse Mn_2O_3 nanocrystals. ACS Catal 2022;12:397–410.
[6] Zhou Z, Sun Z, Duan L. Chemical looping: a flexible platform technology for CH_4 conversion coupled with CO_2 utilization. Curr Opin Green Sustainable Chem 2023; 39:100721.
[7] Krzywanski J, Czakiert T, Nowak W, Shimizu T, Ashraf WM, Zylka A, et al. Towards cleaner energy: an innovative model to minimize NOx emissions in chemical looping and CO_2 capture technologies. Energy 2024;312:133397.
[8] Zylka A, Krzywanski J, Czakiert T, Idziak K, Sosnowski M, Grabowska K, et al. The 4th Generation of CeSFaMB in numerical simulations for CuO-based oxygen carrier in CLC system. Fuel 2019;255:115776.
[9] Yu Z, Yang Y, Yang S, Zhang Q, Zhao J, Fang Y, et al. Iron-based oxygen carriers in chemical looping conversions: a review. Carbon Resources Conversion 2019;2: 23–34.
[10] Cabello A, Abad A, García-Labiano F, Gayán P, de Diego LF, Adánez J. Kinetic determination of a highly reactive impregnated Fe_2O_3/Al_2O_3 oxygen carrier for use in gas-fueled Chemical Looping Combustion. Chem Eng J 2014;258:265–80.
[11] Guan Y, Zhang G, Wang R, Wang Y, Liu Y. Study on the synergistic effect and oxygen vacancy of CeO_2/Fe_2O_3 oxygen carrier for improving reactivity in carbon monoxide chemical looping combustion. Fuel 2024;357:129832.
[12] Wu X, Dong Y, Ma J, Bu H, Su Z, Shen L, et al. Industrial-scaled Cu-Fe composite oxygen carrier for chemical looping combustion through extrusion-spheronization. Chem Eng J 2023;477:146620.
[13] Han Y, Wang H, Huang D, Wang P, Zhang J, Ren X, et al. Crystal facet-dependent reduction behavior of α-Fe_2O_3 in hydrogen atmosphere. Appl Surf Sci 2023;638: 158056.
[14] Liu X, Liu J, Chang Z, Sun X, Li Y. Crystal plane effect of Fe_2O_3 with various morphologies on CO catalytic oxidation. Catal Commun 2011;12:530–4.
[15] Liu Y, Lu F, Tang Y, Liu M, Tao FF, Zhang Y. Effects of initial crystal structure of Fe_2O_3 and Mn promoter on effective active phase for syngas to light olefins. Applied Catalysis B: Environmental. 2020;261:118219.
[16] Gao R, Pan L, Li Z, Shi C, Yao Y, Zhang X, et al. Engineering facets and oxygen vacancies over hematite single crystal for Intensified electrocatalytic H_2O_2 production. Adv Funct Mater 2020;30:1910539.
[17] Hu S, Jiang L, Wang B, Ma Y. Enhanced electrocatalytic methanol oxidation properties by photo-assisted Fe_2O_3 nanoplates. Int J Hydrogen Energy 2019;44: 13214–20.
[18] Yin Y, Zhang Y, Wu B, Hu L, Wang Y, Wan J, et al. Facet-dependent reactivity of α-Fe_2O_3 nanosheet on reactive oxygen species generation in Fenton-like process. Applied Catalysis B: Environmental. 2024;340:123165.
[19] Jin X, Wu D, Liu C, Huang S, Zhou Z, Wu H, et al. Facet effect of hematite on the hydrolysis of phthalate esters under ambient humidity conditions. Nat Commun 2022;13:6125.
[20] Tan W, Liang Y, Xu Y, Wang M. Structural-controlled formation of nano-particle hematite and their removal performance for heavy metal ions: a review. Chemosphere 2022;306:135540.
[21] Alalwan HA, Mason SE, Grassian VH, Cwiertny DM. α-Fe_2O_3 Nanoparticles as oxygen carriers for chemical looping combustion: an Integrated materials characterization approach to understanding oxygen carrier performance, reduction mechanism, and particle size effects. Energy & Fuels 2018;32:7959–70.
[22] Chan JYT, Ang SY, Ye EY, Sullivan M, Zhang J, Lin M. Heterogeneous photo-Fenton reaction on hematite (α-Fe_2O_3){104}, {113} and {001} surface facets. Phys Chem Chem Phys 2015;17:25333–41.
[23] Tang J-J, Liu B. Reactivity of the Fe_2O_3(0001) surface for methane oxidation: a GGA + U study. J Phys Chem C 2016;120:6642–50.
[24] Zhang H-X, Yu X-Y, Su X, Gao X, Huang Z-Q, Yang B, et al. Dopant-Enhanced harmonization of α-Fe_2O_3 oxygen migration and surface catalytic reactions during chemical looping reforming of methane. Chem Eng J 2024;481:148446.
[25] Zhao Y, Yan D, Ding C, Su D, Ge Y, Zhao Y, et al. Fe_2O_3 nanocubes exposed (012) active facets combination with graphene rendering enhanced lithium storage capability. J Power Sources 2016;327:658–65.
[26] Liu X, Zhang J, Wu S, Yang D, Liu P, Zhang H, et al. Single crystal α-Fe_2O_3 with exposed {104} facets for high performance gas sensor applications. RSC Adv 2012; 2:6178–84.
[27] VandeVondele J, Krack M, Mohamed F, Parrinello M, Chassaing T, Hutter J. Quickstep: Fast and accurate density functional calculations using a mixed Gaussian and plane waves approach. Comput Phys Commun 2005;167:103–28.
[28] Perdew JP, Burke K, Ernzerhof M. Generalized gradient approximation made Simple. Phys Rev Lett 1996;77:3865–8.
[29] Naveas N, Pulido R, Marini C, Hernández-Montelongo J, Silván MM. First-principles calculations of hematite (α-Fe_2O_3) by self-consistent DFT+U+V. iScience 2023;26:106033.
[30] Grimme S, Antony J, Ehrlich S, Krieg H. A consistent and accurate ab initio parametrization of density functional dispersion correction (DFT-D) for the 94 elements H-Pu. J Chem Phys 2010;132:154104.
[31] Henkelman G, Uberuaga BP, Jónsson H. A climbing image nudged elastic band method for finding saddle points and minimum energy paths. J Chem Phys 2000; 113:9901–4.
[32] Henkelman G, Jónsson H. A dimer method for finding saddle points on high dimensional potential surfaces using only first derivatives. J Chem Phys 1999;111: 7010–22.
[33] Huang L, Tang M, Fan M, Cheng H. Density functional theory study on the reaction between hematite and methane during chemical looping process. Appl Energy 2015;159:132–44.
[34] Wang Ww X-G, Shaikhutdinov Sh K, Ritter M, Petersen M, Wagner F, Schlögl R, Scheffler M. The hematite (α-Fe_2O_3) (001) surface: evidence for Domains of distinct Chemistry. Phys Rev Lett 1998;81:1038–41.
[35] Blake Reh RL, Zoltai T, Finger LW. Refinement of the hematite structure. Am Mineral 1966;51:123–9.
[36] Momma K, Izumi F. VESTA: a three-dimensional visualization system for electronic and structural analysis. J Appl Crystallogr 2008;41:653–8.
[37] van Duin ACT, Dasgupta S, Lorant F, Goddard WA. ReaxFF: a reactive force field for Hydrocarbons. J Phys Chem 2001;105:9396–409.
[38] Thompson AP, Aktulga HM, Berger R, Bolintineanu DS, Brown WM, Crozier PS, et al. Lammps - a flexible simulation tool for particle-based materials modeling at the atomic, meso, and continuum scales. Comput Phys Commun 2022;271:108171.
[39] Feng Y, Wang P, Wang N, Guo X, Ma S. Sintering mechanism of Fe_2O_3 particles during iron-based chemical looping combustion by using ReaxFF MD simulation and experiments. Energy & Fuels 2024;38:8928–37.
[40] Burger CM, Zhu W, Ma G, Zhao H, van Duin ACT, Ju Y. Experimental and computational investigations of ethane and ethylene kinetics with copper oxide particles for Chemical Looping Combustion, vol. 38. Proceedings of the Combustion Institute; 2021. p. 5249–57.
[41] Meng L, Zhu Y, Zhu M, Wu G, Guo W, Geng C, et al. Exploring depolymerization mechanism and complex reaction networks of aromatic structures in chemical looping combustion via ReaxFF MD simulations. J Energy Inst 2023;107:101180.
[42] Geng S, Han Z, Hu Y, Cui Y, Yue J, Yu J, et al. Methane Decomposition kinetics over Fe_2O_3 Catalyst in Micro Fluidized bed reaction analyzer. Ind Eng Chem Res 2018;57:8413–23.
[43] Ma Z, Liu G, Lu Y, Wang J, Zhang H. Improved redox performance of Fe_2O_3/Al_2O_3 oxygen carrier via element doping in chemical looping combustion. Fuel Process Technol 2021;224.
[44] Jerndal E, Mattisson T, Lyngfelt A. Thermal analysis of chemical-looping combustion. Chem Eng Res Des 2006;84:795–806.
[45] Yin R, Chen J, Mi J, Liu H, Yan T, Shan L, et al. Breaking the activity–selectivity Trade-Off for Simultaneous catalytic elimination of nitric oxide and Chlorobenzene via $FeVO_4$–Fe_2O_3 Interfacial charge transfer. ACS Catal 2022;12:3797–806.
[46] Cheng S, Xu F, Yang S, Zhang B, Song W, Zhu X, et al. Modulating the activity and SO_2 Resistance of α-Fe_2O_3 Catalysts for NH_3–SCR of NOx via crystal facet engineering. Environ Sci Technol 2024;58:8955–65.
[47] Guan Y, Liu Y, Wang B, Feng Y, Lyu Q. Reaction characteristics and lattice oxygen transformation mechanism of semi-coke chemical looping gasification with Fe_2O_3/$CaSO_4$–Al_2O_3 oxygen carrier. J Clean Prod 2022;369:133291.
[48] Xu T, Wang X, Zhao H, Xiao B, Liu D, Liu W. Modulating lattice oxygen activity of $Ca_2Fe_2O_5$ brownmillerite for the co-production of syngas and high purity hydrogen via chemical looping steam reforming of toluene. Applied Catalysis B: Environmental. 2023;320:122010.
[49] Monazam ER, Breault RW, Siriwardane R, Richards G, Carpenter S. Kinetics of the reduction of hematite (Fe_2O_3) by methane (CH_4) during chemical looping combustion: a global mechanism. Chem Eng J 2013;232:478–87.
[50] Dong M, Xiong J, Liu H, Huang Z, Hou H, Liang Y, et al. Microscopic insights into the reaction mechanism of Fe-based oxygen carrier with CH_4 in chemical-looping combustion. Appl Surf Sci 2024;677:161011.
[51] Zhou D, Zhou Y, Li Y, Shen W. Nanostructured iron oxides for heterogeneous catalysis. EnergyChem 2024;6:100124.